

Determination of the scalar polarizabilities of the proton using beam asymmetry Σ_3 in Compton scattering

The A2 Collaboration

V. Sokhoyan^{1,2}, E. J. Downie², E. Mornacchi¹, J. A. McGovern³, N. Krupina¹, F. Afzal⁴, J. Ahrens¹, C. S. Akondi⁵, J. R. M. Annand⁶, H. J. Arends¹, R. Beck⁴, A. Braghieri⁷, W. J. Briscoe², F. Cividini¹, C. Collicott^{1,2,8,9}, S. Costanza⁷, A. Denig¹, M. Dieterle¹⁰, M. Ferretti¹, S. Gardner⁶, S. Garni¹⁰, D. I. Glazier^{6,11}, D. Glowa¹¹, W. Gradl¹, G. Gurevich¹², D. Hamilton⁶, D. Hornidge¹³, G. M. Huber¹⁴, A. Käser¹⁰, V. L. Kashevarov¹, I. Keshelashvili¹⁰, R. Kondratiev¹², M. Korolija¹⁵, B. Krusche¹⁰, V. Lensky^{1,3,16,17}, J. Linturi¹, V. Lisin¹⁸, K. Livingston⁶, I. J. D. MacGregor⁶, R. Macrae⁶, D. M. Manley⁵, P. P. Martel^{1,13,19}, D. G. Middleton^{1,13}, R. Miskimen²⁰, A. Mushkarenkov^{1,18,20}, A. Neiser¹, M. Oberle¹⁰, H. Ortega Spina¹, M. Ostrick¹, P. Ott¹, P. B. Otte¹, B. Oussena^{1,2}, D. Paudyal¹⁴, P. Pedroni⁷, A. Polonski¹², S. Prakhov^{1,2,21}, A. Rajabi²⁰, T. Rostomyan¹⁰, A. Sarty⁹, S. Schumann¹, K. Spieker⁴, O. Steffen¹, I. I. Strakovsky², B. Strandberg⁶, T. Strub¹⁰, I. Supek¹⁵, A. Thiel⁴, M. Thiel¹, A. Thomas¹, M. Unverzagt¹, S. Wagner¹, D. P. Watts¹¹, J. Wettig¹, L. Witthauer¹⁰, D. Werthmüller^{10,6}, M. Wolfes¹, and L. Zana¹

¹ Institut für Kernphysik, Universität Mainz, D-55099 Mainz, Germany

² Department of Physics, The George Washington University, Washington, DC 20052, USA

³ School of Physics and Astronomy, University of Manchester, Manchester, M13 9PL, UK

⁴ Helmholtz-Institut für Strahlen- und Kernphysik, Universität Bonn, D-53115 Bonn, Germany

⁵ Department of Physics, Kent State University, Kent, Ohio 44242, USA

⁶ SUPA School of Physics and Astronomy, University of Glasgow, Glasgow G12 8QQ, UK

⁷ INFN Sezione di Pavia, I-27100 Pavia, Italy

⁸ Department of Physics and Atmospheric Science, Dalhousie University, Halifax, Nova Scotia B3H 4R2, Canada

⁹ Department of Astronomy and Physics, Saint Mary's University, Halifax, Nova Scotia B3H 3C3, Canada

¹⁰ Departement Physik, Universität Basel, CH-4056 Basel, Switzerland

¹¹ School of Physics, University of Edinburgh, Edinburgh EH9 3JZ, UK

¹² Institute for Nuclear Research, 125047 Moscow, Russia

¹³ Department of Physics, Mount Allison University, Sackville, New Brunswick E4L 1E6, Canada

¹⁴ Department of Physics, University of Regina, Regina, Saskatchewan S4S 0A2, Canada

¹⁵ Rudjer Boskovic Institute, HR-10000 Zagreb, Croatia

¹⁶ Institute for Theoretical and Experimental Physics, 117218 Moscow, Russia

¹⁷ National Research Nuclear University MEPhI (Moscow Engineering Physics Institute), 115409 Moscow, Russia

¹⁸ Lebedev Physical Institute, 119991 Moscow, Russia

¹⁹ Laboratory for Nuclear Science, Massachusetts Institute of Technology, Cambridge, Massachusetts 02139, USA

²⁰ Department of Physics, University of Massachusetts Amherst, Amherst, Massachusetts 01003, USA

²¹ Department of Physics and Astronomy, University of California Los Angeles, Los Angeles, California 90095-1547, USA

Received: date January 11, 2017/ Revised version: date

Abstract. The scalar dipole polarizabilities, α_{E1} and β_{M1} , are fundamental properties related to the internal dynamics of the nucleon. The currently accepted values of the proton polarizabilities were determined by fitting to unpolarized proton Compton scattering cross section data. The measurement of the beam asymmetry Σ_3 in a certain kinematical range provides an alternative approach to the extraction of the scalar polarizabilities. At the Mainz Microtron (MAMI) the beam asymmetry was measured for Compton scattering below pion photoproduction threshold for the first time. The results are compared with model calculations and the influence of the experimental data on the extraction of the scalar polarizabilities is determined.

1 Introduction

The proton polarizabilities characterize the inelastic structure of the nucleon [1,2], and thus are complementary to

the electromagnetic form factors that describe the elastic structure. These polarizabilities are fundamental properties of the proton, as much as its mass, charge, and magnetic moment. They contribute at second order in the low-

energy expansion of Compton scattering on the proton ($\gamma p \rightarrow \gamma p$) [3,4], and are the first contributions beyond the low-energy theorem [5,6]. The scalar polarizabilities are of great importance for nuclear and atomic physics, and other related fields, and are currently a significant source of uncertainty in the determination of the proton charge radius from muonic hydrogen Lamb shift [7]. The neutron polarizabilities even play a role in neutron star physics (see e.g. [8]), illustrating the impact of these sub-microscopic properties at macroscopic scales. Furthermore, a precise and model-independent determination of the scalar polarizabilities is crucial for the extraction of the spin polarizabilities. The first measurement of the double polarization asymmetry Σ_{2x} at MAMI and the individual extraction of the proton spin polarizabilities was reported recently [9]. The current values of the scalar polarizabilities of the proton, presented by the Particle Data Group (PDG) [10], are

$$\begin{aligned}\alpha_{E1} &= (11.2 \pm 0.4) \times 10^{-4} \text{ fm}^3 \\ \beta_{M1} &= (2.5 \pm 0.4) \times 10^{-4} \text{ fm}^3.\end{aligned}$$

These values were extracted from the unpolarized cross section of Compton scattering on the proton at energies below 170 MeV, from a large number of experiments, but particularly those of Refs. [11, 12, 13, 14]. By far the largest of these data sets [11] was measured previously at MAMI.

The measurement of the beam asymmetry Σ_3 provides an alternative approach to the extraction of the scalar polarizabilities, with a potentially complementary sensitivity to α_{E1} and β_{M1} . A low-energy expansion of Σ_3 gives [15]

$$\Sigma_3 = \Sigma_3^{(B)} - \frac{4M\omega^2 \cos\theta \sin^2\theta}{\alpha_{em}(1 + \cos^2\theta)^2} \beta_{M1} + \mathcal{O}(\omega^4), \quad (1)$$

where $\Sigma_3^{(B)}$ represents the Born contribution, M is the mass of the target, α_{em} is the fine-structure constant, and ω and θ are the incoming photon energy and the polar angle of the outgoing photon in the Breit frame. The Born term $\Sigma_3^{(B)}$ depends only on the mass, charge, and magnetic moment of the proton. At sufficiently low energies ($\omega \ll m_\pi$), the contribution of the terms at $\mathcal{O}(\omega^4)$ could be neglected and very precise measurements could isolate β_{M1} cleanly. In practice, even though α_{E1} and other terms (such as the pion-pole contribution, in which both photons couple to the nucleon via the exchange of a neutral pion) only enter at $\mathcal{O}(\omega^4)$, for energies above about 80 MeV they are at least as important as β_{M1} [16]. However, in the context of a theoretical prediction for the asymmetry, α_{E1} and β_{M1} can both be fit. In this work, the first results on the beam asymmetry below pion photoproduction threshold are presented and compared with existing theoretical predictions. The influence of the new data on the polarizabilities and the potential of further high-precision measurements are discussed.

2 Experiment

The experiment was performed at the MAMI accelerator facility [17,18] using an electron beam with an energy of

883 MeV. The electron beam passed through a thin diamond radiator, where some of the electrons underwent coherent bremsstrahlung [19,20]. The energy-degraded electrons were then detected in the focal plane of the Glasgow Mainz Photon Tagging Spectrometer [21,22,23]. Using energy conservation, the energy of the resulting photon is determined. The linearly polarized photons traveled down the beamline to the experimental area, where they impinged on a 10-cm-long liquid hydrogen target. The photons were then energy-tagged to the reaction products using a timing coincidence between the tagger and the detector system.

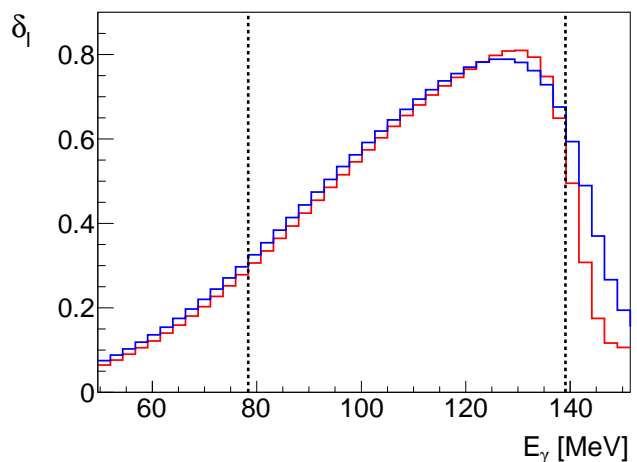


Fig. 1. Degree of linear polarization for two orientations of the diamond with polarization plane parallel (red line) and perpendicular (blue line) to the horizontal lab axis. The black dashed lines indicate the range used in further analysis.

The measurements were performed with two orientations of the diamond, resulting in a relative angle of 90° between the corresponding polarization planes (formed by the momentum of the incoming photon and its electric field vector). The degree of linear polarization was determined directly from the experimental data, by fitting the polarization enhancement obtained from the ratio of the photon energy spectra taken with the diamond and a reference copper radiator. The enhancement was calculated in short time intervals corresponding to the readout of the scaler counters (typically every 1-2 seconds). This event-based method allowed us to account for changes in the values of linear polarization due to small variations in the position of the incoming electron beam. Figure 1 shows the resulting averaged degree of linear polarization for both polarization settings. These values were used in the determination of the beam asymmetry (see Sec. 3). The reaction products were detected by the Crystal Ball/TAPS calorimeter system covering 97% of the full solid angle. The Crystal Ball calorimeter, consisting of 672 NaI crystals, covered polar angles from 20° to 155° [24]. The TAPS forward wall is built of 366 BaF₂ crystals covering polar angles from 4° to 20° , and 72 PbWO₄ crystals covering

the angular range from 1° to 4° [25]. In this work, we used the signal from the Crystal Ball and the BaF₂ crystals. Both Crystal Ball and TAPS detectors have full azimuthal coverage. In addition to these calorimeters, a Particle Identification Detector (PID), consisting of 24 scintillator bars [26], and two Multiwire Proportional Chambers (MWPCs), were incorporated in the Crystal Ball detector system for identification and enhanced tracking of charged particles. In the TAPS region, the charged particles were identified with thin plastic veto scintillators placed in front of the BaF₂ crystals.

In the selection of $\gamma p \rightarrow \gamma p$ events, precisely one neutral hit in the Crystal Ball was required since the outgoing proton did not reach the calorimeters in the relevant energy range ($E_\gamma = 79\text{--}139$ MeV). For the identification of the photon, it was required that no charged hit was identified in the PID or MWPCs. Due to significant contamination of the forward region with electromagnetic background originating from the photon beam, only events with outgoing photon scattering angles $\theta > 30^\circ$ were used in the extraction of the beam asymmetry. In order to reduce the random background in the Crystal Ball, it was required that the scattered photon was time-coincident with the tagger hit within 3 ns. In order to remove randomly coincident events from the selection, we sampled the random background in two timing windows at (-200; -20) ns and (20; 200) ns and subtracted it from the signal after normalization according to the width of the selected time intervals. The data were divided into three incoming photon energy ranges ($E_\gamma = 79\text{--}98$ MeV, $98\text{--}119$ MeV, and, $119\text{--}139$ MeV). For each of these ranges, the energy of the outgoing photons E_γ^{out} had to agree with limits determined from Monte Carlo simulations ($E_\gamma^{\text{out}} = 65\text{--}100$ MeV, $80\text{--}120$ MeV, and $95\text{--}140$ MeV respectively). These limits were defined according to the kinematics of Compton scattering and energy resolution of the Crystal Ball. Furthermore, in order to remove events from the kapton windows of the target vessel and scattering chamber, (positioned along the photon beam), the same analysis procedure was also applied to data taken with an empty target and the contribution of the empty target was scaled and subtracted.

The consideration of the missing mass spectrum before the outgoing photon energy cut, as shown in Fig. 2, allowed us to determine the upper limit of the background contamination in the data (after the application of this cut, the tails in the missing mass spectrum are suppressed, but the signal region remains practically unchanged). The data obtained with each of the two polarization planes (data were also taken with an unpolarized photon beam from a copper radiator) are compared with the spectrum obtained from Monte Carlo simulation of Compton scattering. The agreement of the lineshape between both data sets indicates an absence of strong systematic effects in the unpolarized component of the selected data sample. For all three photon energy ranges used to determine Σ_3 , a missing mass cut of $925 < M_{\text{miss}} < 955$ MeV was applied (see Fig. 2). The shapes of the distributions obtained from the experimental data and Monte Carlo simulation are in

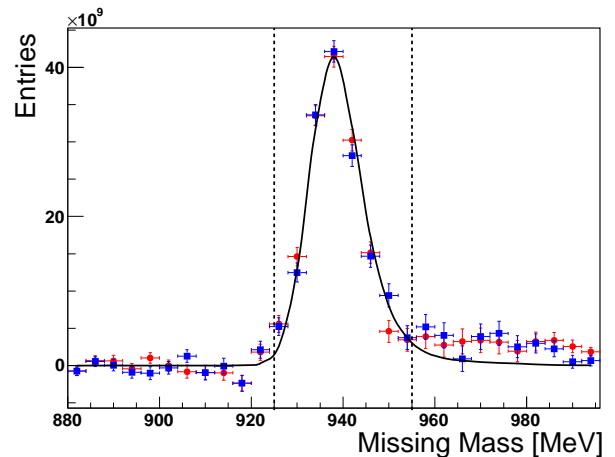


Fig. 2. Missing mass for the incoming photon energy range $79\text{--}98$ MeV and scattered photon polar angles $30^\circ < \theta < 155^\circ$, data were obtained for two polarization planes parallel and perpendicular to the horizontal (red circles and blue squares respectively). The black curve represents the Monte Carlo simulated distribution for Compton scattering, the dashed lines indicate the applied cut.

good agreement, indicating no significant background contamination in the selected range. The overall background in the final data sample, consisting of 200,143 Compton scattering events in the energy range ($79 < E_\gamma < 139$ MeV), with polar angle coverage ($30^\circ < \theta < 155^\circ$), did not exceed 4%. We accounted for the possible influence of the remaining background on the final results in the systematic error (see Sec. 3). Furthermore, in order to test for systematic effects in the identification of Compton scattering events, data were also taken with unpolarized beam from a copper radiator. From these data, the unpolarized cross sections were extracted. The measured unpolarized cross sections agreed well with previous data [11].

3 Beam asymmetry Σ_3

The use of a linearly polarized photon beam with an unpolarized target introduces an azimuthal angle dependence to the cross section. We are interested in the case of two perpendicular polarization directions, corresponding to perpendicular orientations of the diamond crystal. Defining ϕ as the angle between one of the polarization planes and the scattering plane defined by the incoming and outgoing photon momenta, the two cross sections can be written as

$$\sigma_{\text{pol}} = \sigma_{\text{unpol}}(1 \pm \delta_l \Sigma_3 \cos 2\phi), \quad (2)$$

where σ_{unpol} is the cross section for an unpolarized photon beam and δ_l is the degree of linear polarization of the beam. The beam asymmetry Σ_3 determines the magnitude of the modulation. The top two panels of Fig. 3 show sample ϕ distributions, in which the $\cos 2\phi$ modulation can be clearly identified.

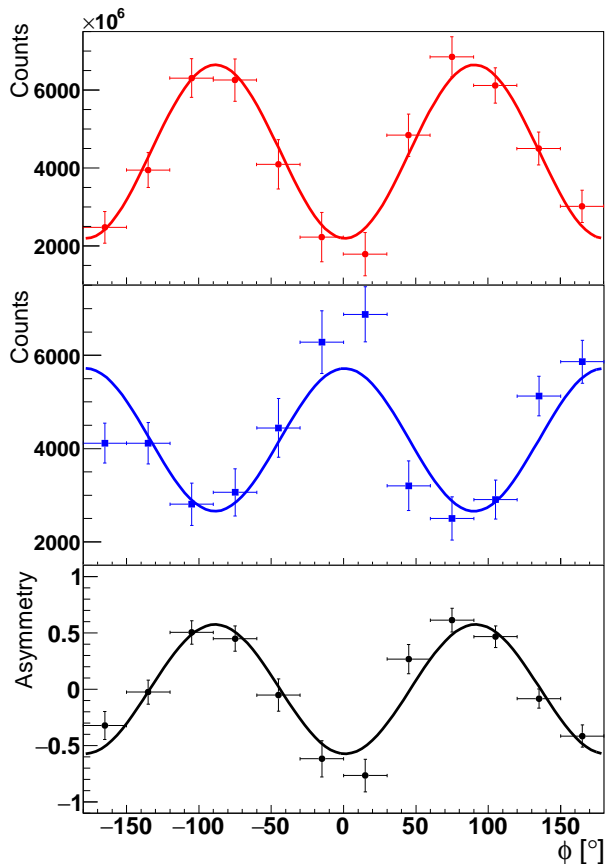


Fig. 3. Sample ϕ distributions of the outgoing photon. The upper two panels show ϕ distributions obtained with polarization plane parallel (upper) and perpendicular to (middle) the horizontal lab axis. The lower-most panel shows the ϕ -dependent asymmetry obtained from Eq. 4.

At $\phi = 0^\circ$ the photon polarization is either parallel or perpendicular to the scattering plane, with corresponding cross sections denoted σ_{\parallel} and σ_{\perp} , giving the usual expression for Σ_3 :

$$\Sigma_3 \equiv \frac{\sigma_{\parallel} - \sigma_{\perp}}{\sigma_{\parallel} + \sigma_{\perp}}. \quad (3)$$

In order to account for different polarization values for the sets corresponding to the two different orientations of the diamond, the corresponding number of Compton scattering events was weighted with the corresponding linear polarization values (where the $\Sigma_3 \cos 2\phi$ term follows from Eq. 2):

$$\Sigma_3 \cos(2(\phi + \phi_0)) = \frac{\sigma_{\parallel} - \sigma_{\perp}}{\delta_{\perp}\sigma_{\parallel} + \delta_{\parallel}\sigma_{\perp}} = \frac{N_{\parallel} - N_{\perp}}{\delta_{\perp}N_{\parallel} + \delta_{\parallel}N_{\perp}}, \quad (4)$$

here δ_{\parallel} and δ_{\perp} represent the degree of polarization for the two polarization settings respectively, and N_{\parallel} and N_{\perp} represent the event rates for the two polarization settings measured in the experiment. The effect of a possible deviation of the polarization planes from the expected positions (e.g. due to geometrical positioning of the radiator) was

accounted for by fixing the phase of the azimuthal angle to the value determined by fitting the experimental data ($\phi_0 = (-1 \pm 1)^\circ$). The bottom panel of Fig. 3 shows the angle-dependent asymmetry obtained according to Eq. 4; the $\cos 2\phi$ modulation is again clearly seen.

The beam asymmetry was extracted by fitting the ϕ distributions and equating to $(3/\pi)\Sigma_3 \cos(2(\phi + \phi_0))$ in Eq. 4. The prefactor of $\sin(\Delta\phi)/\Delta\phi = (3/\pi)$ accounts for the damping of the amplitude of the modulation from averaging over bins of width $\Delta\phi = 30^\circ$. The results are shown in Fig. 4 for various ranges of the incoming photon energy and polar angle of the scattered photon. The error bars shown are statistical; the systematic errors are presented as red bars. The most significant contribution to the systematic error is due to the normalization of the photon flux (typically in order of 15% at low energies and 4% at higher energies). The next most significant source of uncertainty is background contamination, which was estimated based on the events outside (on the right) of the missing mass peak (increasing up to 50% at low and high polar angles and being in order of 3% for central angular bins). Another source of uncertainty is the determination of the degree of polarization. Generally, the influence of this effect is small (typically below 2%) compared to the other effects. The combination of the effects described above results in the systematic error shown in Fig. 4.

In addition, Fig. 4 also shows a comparison between the data and various calculations. The solid line shows only the Born term (see Eq. 1), which is independent of all proton structure except the anomalous magnetic moment. Fig. 4 also shows predictions for the asymmetry from Dispersion Relations (DR, dotted) [27, 28] and from two variants of Chiral Perturbation Theory: Baryon Chiral Perturbation Theory (BChPT, dashed) [29] and Heavy Baryon Chiral Perturbation Theory (HBChPT, dash-dotted) [16]. In the former variant the nucleon is treated relativistically whereas in the latter an expansion of the amplitudes in powers of the inverse nucleon mass is performed; in addition the latter calculation is carried out to one order higher in their common power-counting than the former. Both include the contribution of the Delta isobar. In each of these calculations the spin polarizabilities are not free parameters, but predictions of the theory (their values can be found in [16, 30, 28] and in particular are summarized in table IV of [30]). However a check within the BChPT framework showed that at the present level of accuracy the choice of the spin polarizabilities has no noticeable influence on the fit to the data of Fig. 4.

The data are in good agreement with the results obtained in all theories. At the same time, the clear separation between the data and the contribution of the Born term, particularly in the energy range $E_{\gamma} = 119\text{--}139$ MeV, indicates the sensitivity of the data to dynamical effects including but not limited to the scalar polarizabilities.

Rather than taking the polarizability values from elsewhere, they can be fit directly to the asymmetry data; however the current precision means that such an extraction will not be competitive. A two-parameter fit gives values of both α_{E1} and β_{M1} , but to minimize the uncertainty

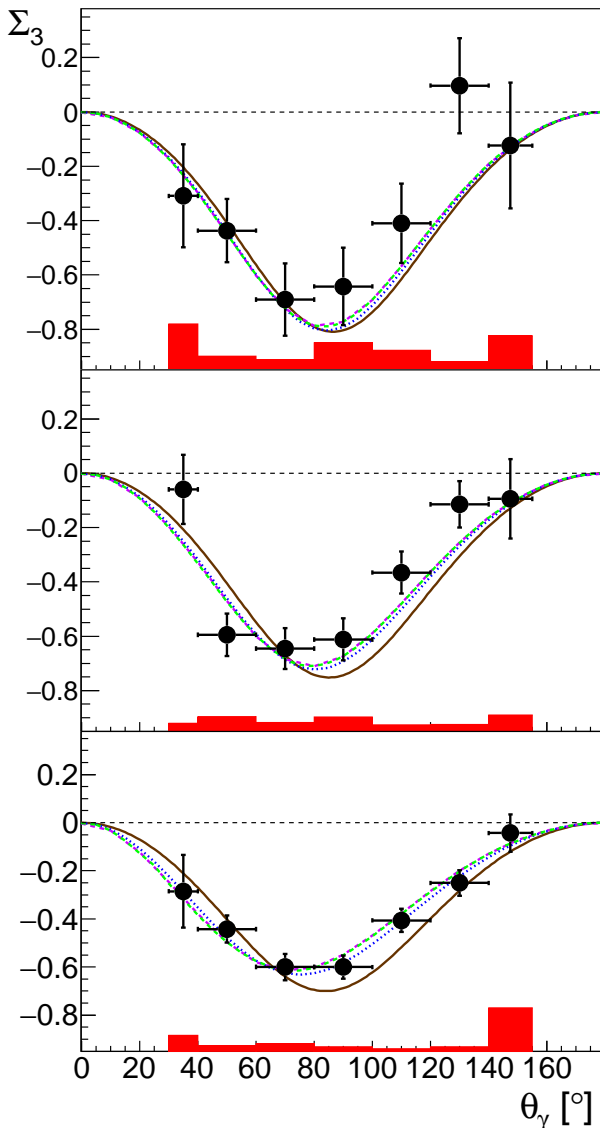


Fig. 4. Beam asymmetry Σ_3 for three energy ranges (uppermost: 79–98 MeV, middle: 98–119 MeV, lowermost: 119–139 MeV). The errors represent statistical errors, the red bars indicate the systematic error. Green dashed curve: BChPT calculation [29], magenta dashed-dotted: DR calculation [27, 28], blue dotted: HBChPT [16], all with $\alpha_{E1} = 10.65 \times 10^{-4} \text{ fm}^3$ and $\beta_{M1} = 3.15 \times 10^{-4} \text{ fm}^3$; brown solid: Born term (curves correspond to the central values of the shown energy bins).

we prefer to use the well-established value $\alpha_{E1} + \beta_{M1} = 14.0 \times 10^{-4} \text{ fm}^3$ obtained from the Baldin sum rule [31] and perform a one-parameter fit, giving a value for $\alpha_{E1} - \beta_{M1}$ or, equivalently, β_{M1} .

The fit was performed using only the new data on the beam asymmetry within the BChPT [29, 30, 32] and HBChPT frameworks [16] (combining the statistical and the systematic errors quadratically), with respective results $\beta_{M1} = 2.8_{-2.1}^{+2.3} \times 10^{-4} \text{ fm}^3$ ($\chi^2/ndf = 19.2/20$) and $\beta_{M1} = 3.7_{-2.3}^{+2.5} \times 10^{-4} \text{ fm}^3$ ($\chi^2/ndf = 17.1/20$); the error

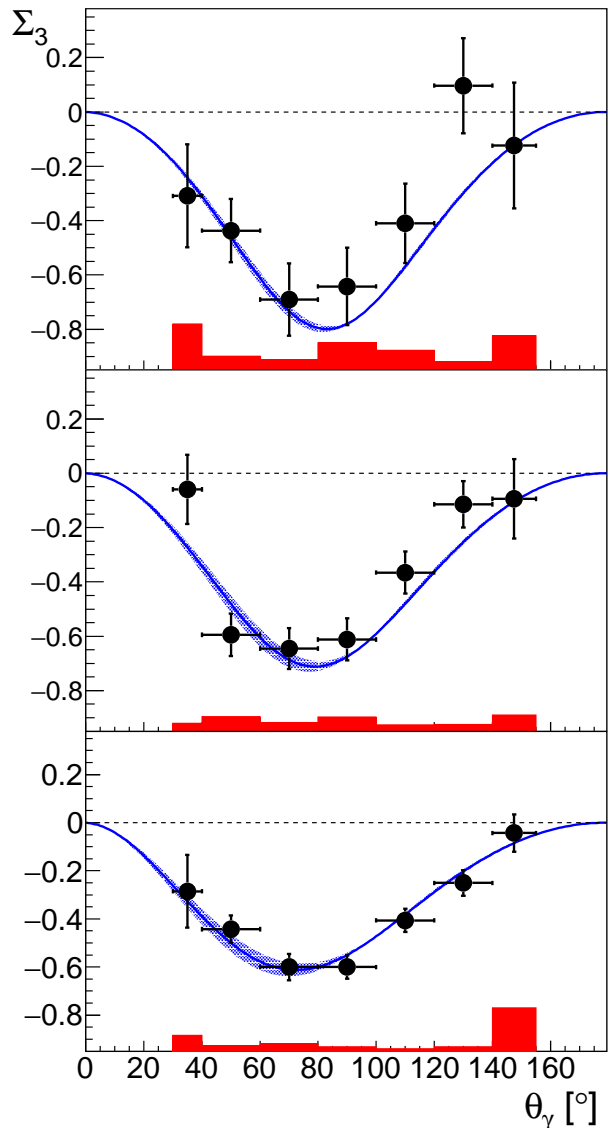


Fig. 5. The result of the fit within BChPT framework obtained by averaging the numerator and denominator in Eq. 4 over angle and energy (blue curve). Shaded bands are determined by the error in β_{M1} . Notation for the data as in Fig. 4.

is obtained from the $\chi^2_{min} + 1$ interval. Because of the finite bin widths, theoretical predictions for the asymmetries, which are ratios of the difference and sum of the two polarized differential cross sections (see Eq. 4), have been obtained by averaging the numerator and denominator over angle (weighted by $\sin \theta$) and energy. Because the asymmetry varies quite rapidly with angle, this makes a noticeable difference to the results.

Figure 5 shows the BChPT result, and the sensitivity of the beam asymmetry to the magnetic polarizability β_{M1} is indicated by the width of the shaded band. The corresponding plot for the HBChPT fit is very similar.

The results for β_{M1} obtained within both frameworks are compatible with each other and also agree with the

$\beta_{M1} = (2.5 \pm 0.4) \times 10^{-4} \text{ fm}^3$ provided by the PDG [10]. Despite the fact that presently the large errors mean that our determination is not competitive and does not significantly impact a global determination, the results indicate that the observable Σ_3 provides new input for the determination of the magnetic polarizability β_{M1} . In order to achieve high accuracy, new high-precision measurements are foreseen at MAMI both with significantly higher statistics and with improved control over systematic effects (e.g. due to the photon flux normalization and very stable linear polarization). The new measurement will follow the ongoing upgrade of the Crystal Ball/TAPS setup at MAMI and the beam asymmetry and unpolarized cross sections will be determined with unprecedented precision.

4 Summary

We have reported on the first measurement of the beam asymmetry Σ_3 for Compton scattering below pion production threshold. The results confirm the existing theoretical predictions (ChPT, HBChPT, DR), and deviate notably from the Born term in which the contributions of the polarizabilities are not included. The results obtained show that the extraction of the scalar polarizabilities from the beam asymmetry as an alternative to the extraction from the unpolarized cross sections is possible, and challenge us to obtain higher-statistics data sets for this observable. In the future, new high-precision measurements both for the beam asymmetry and unpolarized cross section will be performed at MAMI.

We wish to acknowledge the outstanding support of the accelerator group and operators of MAMI. We also acknowledge the contributions and suggestions of H. Grißhammer, V. Pascalutsa, and B. Pasquini to this work. We thank the students of Mount Allison University and The George Washington University for their contributions to the experiment. We acknowledge support from the Collaborative Research Center (CRC) 1044 and Schweizerischer Nationalfonds. The research leading to these results has received funding from the European Community's Seventh Framework Programme FP7/2007-2013 under Grant Agreement Nr. 227431. V. Sokhoyan acknowledges the support of the Carl-Zeiss-Stiftung. We also acknowledge support from the Natural Sciences and Engineering Research Council of Canada (NSERC) FRN: SAPPJ-2015-00023. This work was also supported by the UK Science and Technology Facilities Council (ST/J00175/1, ST/G008604/1, ST/G008582/1, ST/J00006X/1). This material is based upon work supported by the U.S. National Science Foundation under Grant Numbers PHY-1309130, IIA-1358175, and the U.S. Department of Energy (Offices of Science and Nuclear Physics, Award Nos. DE-FG02-99-ER41110, DE-FG02-88ER40415, DE-FG02-01-ER41194).

References

1. V. Bernard, N. Kaiser and U.-G. Meißner, *Int. J. Mod. Phys. E* **4**, 193 (1995).
2. F. Hagelstein, R. Miskimen, V. Pascalutsa, *Prog. Part. Nucl. Phys.* **88**, 29-97 (2016).
3. B. R. Holstein, *Nucl. Phys.* **546**, 213 (1992).
4. D. Babusci, G. Giordano, A. I. L'vov, G. Matone, and A. M. Nathan, *Phys. Rev. C* **58**, 1013 (1998).
5. F. E. Low, *Phys. Rev.* **96**, 1428 (1954).
6. M. Gell-Mann and M. L. Goldberger, *Phys. Rev.* **96**, 1433 (1954).
7. Aldo Antognini et al., *Science* **339**, 417 (2013).
8. J. Bernabeu, Torleif Erik Oskar Ericson, and C. Ferro Fontan, *Phys.Lett. B* **49**, 381-384 (1974).
9. P. P. Martel et al., *Phys. Rev. Lett.* **114**, 112501 (2015).
10. K. A. Olive et al. (Particle Data Group), *Chin. Phys. C* **38**, 090001 (2014).
11. V. Olmos de Leon et al., *Eur. Phys. J. A* **10**, 207-2013215 (2001).
12. F. J. Federspiel et al., *Phys. Rev. Lett.* **67**, 1511 (1991).
13. B. E. MacGibbon et al., *Phys. Rev. C* **52**, 2097 (1995).
14. A. Zieger et al., *Phys. Lett. B* **278**, 34 (1992).
15. N. Krupina, V. Pascalutsa, *Phys.Rev.Lett.* **110**, 262001 (2013).
16. J.A. McGovern, D.R. Phillips, H.W. Grißhammer, *Eur. Phys. J. A* **49**, 12 (2013).
17. K.-H. Kaiser et al., *Nucl. Instrum. Methods A* **593**, 159 (2008).
18. A. Jankowiak, *Eur. Phys. J. A* **28**, 149 (2006).
19. U. Timm, *Fortschr. Phys.* **17**, 765 (1969).
20. D. Lohmann et al., *Nucl. Instrum. Methods A* **343**, 494 (1994).
21. I. Anthony et al., *Nucl. Instrum. Methods A* **301**, 230 (1991).
22. S. Hall et al., *Nucl. Instrum. Methods A* **368**, 698 (1996).
23. J. C. McGeorge et al., *Eur. Phys. J. A* **37**, 129 (2008).
24. A. Starostin, B. M. K. Nefkens, et al. (The Crystal Ball Collaboration), *Phys. Rev. C* **64**, 055205 (2001).
25. R. Novotny, *IEEE Trans. Nucl. Sci.* **38**, 379 (1991).
26. D. Watts, The Crystal Ball and TAPS detectors at the MAMI electron beam facility, in *Proceedings of the 11th International Conference on Calorimetry in Particle Physics (Color2004)*, Perugia, Italy 2004 (*World Scientific, 2005*) (World Scientific, 2004), Vol. 560.
27. D. Drechsel, M. Gorchtein, B. Pasquini, M. Vanderhaeghen, *Phys. Rev. C* **61**, 015204 (1999).
28. B. Pasquini, D. Drechsel, M. Vanderhaeghen, *Phys. Rev. C* **76**, 015203 (2007).
29. V. Lensky and V. Pascalutsa, *Eur. Phys. J. C* **65**, 195 (2010).
30. V. Lensky, J. A. McGovern, V. Pascalutsa, *Eur. Phys. J. C* **75**, 604 (2015).
31. O. Gryniuk, F. Hagelstein, and V. Pascalutsa, *Phys. Rev. D* **92**, 074031 (2015).
32. V. Lensky and J. A. McGovern, *Phys. Rev. C* **89**, 032202 (2014).